How to cite: *Angew. Chem. Int. Ed.* **2024**, *63*, e202414600
doi.org/10.1002/anie.202414600

Electrocatalytic CO_2 Reduction

Engineering a Cu-Pd Paddle-Wheel Metal–Organic Framework for Selective CO_2 Electroreduction

Ruirui Zhang, Yan Liu, Pan Ding, Juanjuan Huang, Martin Dierolf, Shelly D. Kelly, Xinqi Qiu, Yishuo Chen, Mian Zahid Hussain, Weijin Li, Hana Bunzen, Klaus Achterhold, Franz Pfeiffer, Ian D. Sharp, Julien Warnan,* and Roland A. Fischer**

Abstract: Optimizing the binding energy between the intermediate and the active site is a key factor for tuning catalytic product selectivity and activity in the electrochemical carbon dioxide reduction reaction. Copper active sites are known to reduce CO_2 to hydrocarbons and oxygenates, but suffer from poor product selectivity due to the moderate binding energies of several of the reaction intermediates. Here, we report an ion exchange strategy to construct Cu–Pd paddle wheel dimers within Cu-based metal–organic frameworks (MOFs), $[Cu_{3-x}Pd_x(BTC)_2]$ (BTC = benzentricarboxylate), without altering the overall MOF structural properties. Compared to the pristine Cu MOF ($[Cu_3(BTC)_2]$, HKUST-1), the Cu–Pd MOF shifts CO_2 electroreduction products from diverse chemical species to selective CO generation. In situ X-ray absorption fine structure analysis of the catalyst oxidation state and local geometry, combined with theoretical calculations, reveal that the incorporation of Pd within the Cu–Pd paddle wheel node structure of the MOF promotes adsorption of the key intermediate COOH* at the Cu site. This permits CO-selective catalytic mechanisms and thus advances our understanding of the interplay between structure and activity toward electrochemical CO_2 reduction using molecular catalysts.

Introduction

Efficient electrochemical conversion of carbon dioxide (CO_2) into valuable carbon-based feedstocks not only enables the storage of intermittent renewable electricity in chemical bonds but also helps mitigating greenhouse gas emissions.[1] Copper-based catalysts have exhibited remarkable performance in converting CO_2 into a diverse range of hydrocarbon products.[2] Nevertheless, they suffer from insufficient catalytic activity and selectivity toward specific products, which is a consequence of the moderate binding energies of several reaction intermediates on the surface of Cu.[3] Among the various C-based products of the reduction of CO_2, carbon monoxide (CO) holds particular interest due to its substantial usage in the chemical industry and intermediate role in forming hydrocarbon fuels.[4] In aqueous solutions, the two-electron reaction formation of CO from is often hindered by the more kinetically favorable hydrogen (H_2) evolution reaction (HER), resulting in low CO selectivity.[5] Transition metal-based single atom cata-

[*] R. Zhang, X. Qiu, Y. Chen, M. Z. Hussain, Dr. W. Li, Dr. J. Warnan, Prof. R. A. Fischer
Chair of Inorganic and Metal-Organic Chemistry, Department of Chemistry and TUM School of Natural Sciences
Technical University of Munich
Lichtenbergstraße 4, D-85748 Garching, Germany
E-mail: julien.warnan@tum.de
roland.fischer@tum.de

Dr. Y. Liu
College of Chemistry and Materials Science
Anhui Normal University
Wuhu, Anhui, 241000 P. R. China
E-mail: ly0201@ahnu.edu.cn

Dr. P. Ding, Prof. I. D. Sharp
Walter Schottky Institute and TUM School of Natural Sciences
Technical University of Munich
Am Coulombwall 4, 85748 Garching, Germany

Dr. J. Huang, Dr. S. D. Kelly
X-ray Science Division and Advanced Photon Source
Argonne National Laboratory
9700 South Cass Avenue, Lemont, IL 60439, USA

Dr. M. Dierolf, Dr. K. Achterhold, Prof. F. Pfeiffer
Chair of Biomedical Physics, Department of Physics and TUM School of Natural Sciences
Technical University of Munich
85748 Garching, Germany

Dr. H. Bunzen
Chair of Solid State and Materials Chemistry and Institute of Physics
University of Augsburg
86159 Augsburg, Germany

Prof. R. A. Fischer
Catalysis Research Center
Technical University of Munich
Ernst-Otto-Fischer-Str.1, 85748 Garching, Germany

lysts (i.e., Co, Ni),[6] as well as Ag and Au nanoparticles,[7] are highly effective in selectively reducing CO_2 to CO, with faradaic efficiencies (FEs) above 90%. This high FE is mainly ascribed to the moderate binding energies of CO_2 reduction reaction (CO_2RR) intermediates, such as adsorbed COOH and CO.[8] Unfortunately, such catalysts are energy-intensive and costly often involving high temperature synthesis, harsh pyrolysis preparation conditions, or considerable usage of noble metals.

For Cu-based catalysts, several methods have been investigated for enhancing the CO_2 electroreduction efficiency, including morphology regulation[9] and surface modification,[10] as well as use of metal oxide pre-catalysts,[11] single atom centers,[12] and bimetallic alloys.[3a] Notably, Cu-based bimetallic catalytic systems hold significant promise, having shown high efficiency due to synergistic effects ascribed to variations in the work functions of the metals and electron density on the surface of copper.[13] In this regard, the Pd–Cu alloy is one of the most popular candidates for selective CO_2RR as the presence of neighboring Pd atoms alters the adsorption strengths of reaction intermediates and enhancing product selectivity.[14] However, for a solid alloy, active sites are dispersed only on its surface, resulting in reduced reactant accessibility and a limited atomic economy. Achieving a well-defined local structure of porous catalysts is crucial for fundamental understanding and designing highly selective catalytic active sites, as well as for maximizing the noble metal atom efficiency.[15]

Metal–organic frameworks (MOFs) are a class of crystalline porous materials composed of metal ion-containing nodes and organic linkers, enabling custom design of atomic-level active metal sites in terms of electronic properties, structure, and local coordination space.[16] Specifically, the utilization of bimetallic nodes as catalytic sites within MOFs offers several advantages in terms of surface area and tailored structure compared to bimetallic solid state materials.[17] A high concentration of well-defined active sites can be homogeneously distributed within the porous framework, while also being accessible for driving catalytic reactions. Furthermore, the atomically precise structure of these sites enables theoretical investigations and predictions of the underlying catalytic mechanisms.[18] As a consequence of these powerful advantages, bimetallic MOFs have been widely investigated for the oxygen evolution reaction.[19] For the CO_2RR, recent investigations have demonstrated that two-dimensional conjugated MOFs based two metals such as ZnCu[20] and NiFe[21] not only provide good electronic conductivity but also exhibit tunable CO product selectivity. To achieve more cost-effective ligand-coordinated three-dimensional (3D) MOF particles, HKUST-1[22] and its bimetallic blends[23] have also been employed in the electroreduction of CO_2 to yield CH_3OH and C_2H_5OH. Nevertheless, when compared with ultrathin two-dimensional nanosheet materials, MOF particles still suffer from sluggish mass transfer rates of reactants and products in electrolyte.[24] Consequently, designing 3D MOF particle electrocatalysts with an abundance of accessible high-activity sites on their surfaces is highly desirable.

From the above perspective, the post-synthetic metal exchange synthesis of nanostructured MOFs containing structural Cu–Pd dimers can be an ideal approach since it achieves the essential CuPd alloy unit while affording a high concentration of well-defined active metal sites. In this work, we devise atom precise Cu–Pd dimers within a MOF structure with the aim of enhancing electrocatalytic CO production selectivity. Cu–Pd dimers were formed in the paddle-wheel node of the parent structure $[Cu_3(BTC)_2]$ (HKUST-1; BTC = benzenetricarboxylate) through a facile cation exchange process between framework Cu^{2+} and Pd^{2+} to produce a series of samples with systematic compositional variations of Cu–Cu and Cu–Pd dimers. A significant increase in the FE for CO production was observed, increasing from 28.7% to 84.8% at −0.77 V *vs* reversible hydrogen electrode (RHE) in CO_2-saturated 0.5 M $KHCO_3$ upon introduction and increasing the concentration of Cu–Pd dimers. A combination of in situ X-ray absorption spectroscopy (XAS) and density functional theory (DFT) calculations were used to determine the chemical nature of Pd^{2+} sites within the Pd/HKUST-1 structure, thereby allowing the identification of the interactions between reaction intermediates and the modified Cu site.

Results and Discussion

HKUST-1 comprises a tetratopic Cu–Cu dimer paddle wheel node and tritopic benzene-1,3,5-tricarboxylate linkers for coordination. The synthesis of pristine HKUST-1 (HP-0; 0 wt% Pd) was achieved following previously published literature using copper (II) nitrate trihydrate, trimesic acid, and polyvinylpyrrolidone (PVP) (Figure 1a).[25] Mixed-metal HKUST-1 derivatives were produced using an ion exchange method to partly replace Cu^{2+} by Pd^{2+} in the node of the framework. In brief, 600 mg of HP-0 powder and X mg (X = 40, 120 and 200) of palladium acetate were mixed in *N*,*N*-dimethylformamide (DMF) solution in a round-bottom flask wrapped in aluminum foil. After heating at 60 °C for 12 h, the corresponding powders were filtered off and isolated as sea green samples denoted as HP-1, HP-2, and HP-3.

The Pd loadings In the Pd/HKUST-1 samples, obtained by inductively coupled plasma mass spectrometry (ICP-MS), were 1.2, 2.1 and 4.8 wt% Pd, for HP-1, HP-2 and HP-3, respectively. Powder X-ray diffraction (PXRD) analysis (Figure S1) confirmed the phase-purity of HP-0 while diffraction patterns of the functionalized samples remained unaffected by the Pd^{2+} introduction procedure implying that the structural integrity was globally preserved. Notably, no additional reflections corresponding to Pd (111) or Pd (200) were observed near 40.2° or 46.7° in the XRD patterns, nor was palladium acetate detected in the sample. This suggests that the samples do not contain crystalized metallic Pd(0) and that the Pd^{2+} species might be incorporated at the Cu paddle wheel structure.[26] N_2 adsorption-desorption experiments at 77 K for HP-0 (Figures S2,3 and Table S1) revealed a Brunauer–Emmett–Teller (BET) surface area of about 1685 m^2/g. Specific surface areas of ~1586, 1474, and 1220 m^2/g were obtained for HP-1, HP-2, and HP-3,

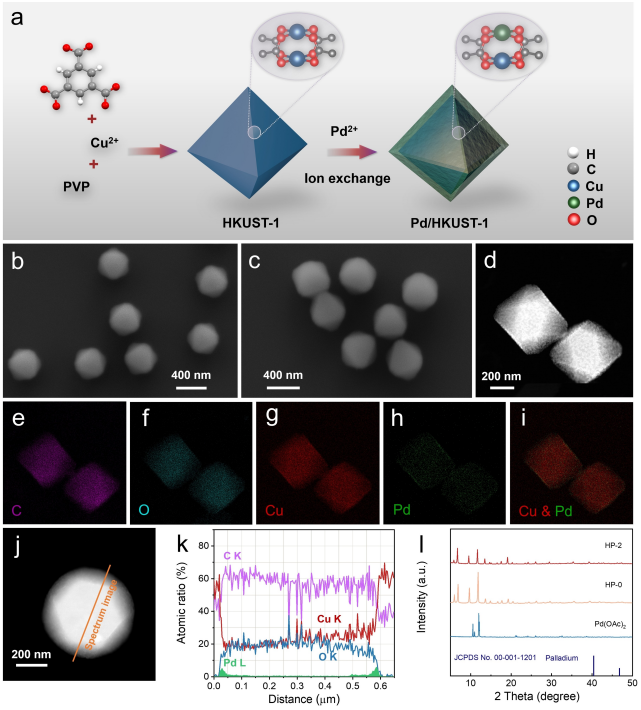

Figure 1. (a) Synthesis scheme of the Pd/HKUST-1. SEM images of (b) HP-0 and (c) HP-2. Electron microscopy analysis of HP-2: (d) Scanning transmission electron microscopy (STEM) image. (e-i) EDX mapping images for C, O, Cu, Pd and CuPd overlay, respectively. (j-k) EDX line scan across the particle, with the depicted intensity profiles of the Cu, C, O, and Pd elements. (l) X-ray diffraction patterns of HP-0 and HP-2.

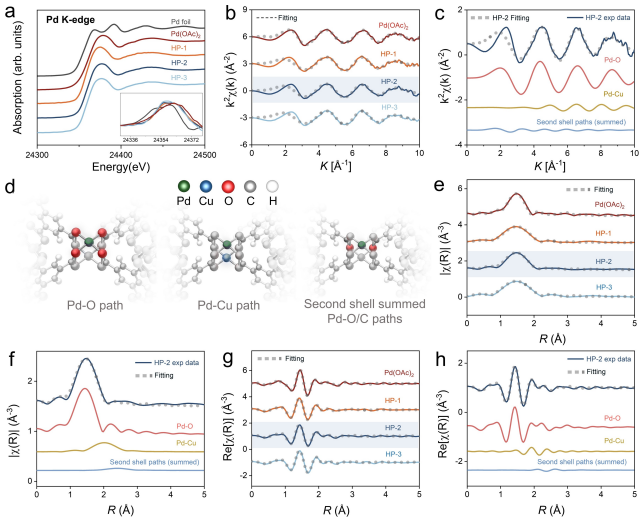

Figure 2. Pd K-edge XAFS spectra: (a) Pd K-edge XANES spectra, and the inset shows the derivatives of the absorption edges. (b) *k* space of Pd EXAFS data (*k* stands for the wave number of the photo-electron involved in the X-ray absorption procedure). The grey dashed lines represent the fitted Pd EXAFS data. (c) The modulus part and (e) the real part of the Fourier-transformed (FT−) EXAFS signals in *R* space. (d) Scheme of Pd–C, Pd-O–C and Pd–O paths. (f), (g) and (h) show the path components used to fit the HP-2 EXAFS signals in *k* space, the modulus and the real part of the FT-EXAFS in *R* space, respectively. The second-shell Pd–C, PdnO–C and Pd–O paths are summed together for a simplified presentation. The fitting paths for HP-1 and HP-3 can be found in the Supporting Information.

respectively. These suggest that the increasing of Pd incorporation brings geometry change in metal nodes and minor restructuring of pores. Scanning electron microscopy (SEM) revealed highly dispersed particle HP samples, possessing uniform octahedral-like shapes with an average size of approximately 600 nm (Figures 1b, c) with no obvious metallic Pd nanoparticles. Energy-dispersive X-ray spectroscopy (EDX) mapping shown in Figures 1e-j confirmed successful Pd integration and that Cu, C, O, and Pd elements are uniformly dispersed in HP-2 surface and the EDX mapping of HP-0 can be found in Figure S4. Interestingly, an associated EDX line scan across an individual HP-2 particle revealed the presence of the Pd signal prominently within approximately 100 nm of the edge of the particle, thereby affirming the surface enrichment of Pd. The same phenomenon can be observed in HP-1 and HP-3 (Figures S5–S7). Taken together, these findings suggest that the post-synthetic modification method results in the incorporation of Pd species into metal nodes that primarily reside in the exterior portions of the obtained Pd/HKUST-1 samples, resulting in a single-metal (Cu) core and bi-metal (Pd/Cu) shell structure.

To investigate the oxidation states and the local structures of the framework-incorporated Pd sites X-ray absorption spectroscopy was performed. Figure 2a shows the X-ray absorption near edge structure (XANES) data of HP-1, HP-2 and HP-3 compared to two references, i.e., Pd foil and $Pd(OAc)_2$. The inset shows the derivatives of the absorption edges. The Pd XANES of HP-2 closely resembles that of $Pd(OAc)_2$, suggesting a Pd oxidation state of +2. Conversely, the first maximum of the derivative of Pd foil displays at a notably lower energy, which is ascribed to its lower oxidation state of 0. The XANES spectra of Pd also show distinctly different XANES spectra compared with HP-1, HP-2 and HP-3. This, combined with XRD results and STEM images, suggests no metallic Pd (small clusters or nanoparticles) was formed in the HP samples. Figure 2b presents the extended X-ray absorption fine structure (EXAFS) plotted in *k* space to gain more insights about the arrangement of atoms surrounding the absorbing atoms. The modulus and the real part of the Fourier transformed EXAFS spectra at the Pd K-edge are plotted in Figures 2c and 2e, respectively, with paths shown in Figure 2d.

To extract coordination shells and bond lengths, quantitative EXAFS analysis was conducted using Athena and Artemis software.[27] We used DFT-optimized structure as the input file to extract five fitting paths as our EXAFS fitting model: the first-shell Pd–O path and Pd–Cu path and the second-shell Pd–C, Pd–O–C and Pd–O paths (as the Scheme shown in Figure 2e). The results are presented in Table S2 and the fitting paths used for HP-2 in the Figure 2f, g, h as examples. Note that the second-shell paths are summed together for a simplified presentation. The fitting paths for HP-1 and HP-3 EXAFS fitting can be found in the Supporting Information. In the modulus part of the FT-EXAFS (Figure 2f), the contribution from the Pd–Cu path at 2 Å is difficult to discern. This is due to the partially

destructive interference between the Pd–Cu and Pd–O paths, resulting in a decreased modulus as observed in the measured spectrum. Consequently, the real part of the FT-EXAFS is plotted to facilitate the identification of signal contributions from the Pd–Cu path.

In addition to this model, we analyzed two other EXAFS fitting models to consolidate the validation of our current model (see Section 2.2 in Supporting Information). Model A excludes the Pd–Cu path. This model significantly degrades the fitting results, indicated by increased reduced chi-square (RCS) and R-factor, and an unreasonable σ^2 value for second-shell C and O. In addition, a *k*-weight analysis in the Supporting Information further indicates that a metal neighbor exists in the first shell.[28] Another model, model B, includes both Pd–Cu, Pd–Pd path. The fitting results show no improvement in this model, as indicated by coordination numbers for Pd–Pd paths being consistently zero. This, along with increased RCS values and expanded error bars for coordination numbers and σ^2, suggests that the Pd–Pd path in the EXAFS fitting model is suboptimal compared to that of the Cu–Pd path. This indicates that the paddlewheel structures in HP-1, HP-2, and HP-3 exhibit a tendency to form Pd–Cu dimers rather than Pd–Pd dimers.

The electrochemical CO_2RR performance of the bimetallic HP-1, HP-2, HP-3 and monometallic HP-0 catalysts were evaluated in an H-type cell using a three-electrode configuration to determine the impact of the Pd–Cu dimers. Pt foil and Ag/AgCl were used as counter and reference electrodes, respectively. The working electrode was prepared by dispersing MOF powders in isopropanol, without the addition of binder such as Nafion, and subsequently casting them onto carbon paper support. All measurements were performed in a CO_2-saturated 0.5 M $KHCO_3$ aqueous electrolyte solution (pH = 7.2) with the flow rate of CO_2 gas maintained at 40 sccm using a mass flow controller. The gaseous products were measured using online gas chromatography (GC).

The Figure of merits of CO_2RR with different catalysts in CO_2-saturated electrolytes are presented in Figure 3, extracted from the corresponding the linear sweep voltammetry (LSV) curves (Figure S8). A notable increase in current density was observed in the CO_2-saturated electrolyte, suggesting a preference for CO_2RR over HER with these catalysts with on onset potential at ~−0.47 V_{RHE}. Relative to the Pd-free HP-0 catalyst, all bimetallic catalysts (HP-1 to HP-3) exhibited enhanced selectivity toward CO production (Figure 3a). At an applied potential of −0.77 V_{RHE}, HP-0 exhibited a FE for CO of ~28 %, while HP-1 and HP-3 exhibited FEs of approximately 45 % and 70 %, respectively. The maximum FE for CO production of ~85 % was achieved with HP-2 and corresponds to a two-fold increase relative to that of HP-1. EDX line scan results shown in Figure 1k and Figure S7 indicate that HP-2 possesses a bimetallic shell thickness of approximately 100 nm, larger than that of HP-1 (~20 nm) but less than HP-3 (~120 nm). The superior performance of HP-2 may be attributed to this optimal shell thickness (relative to HP-1) and its more uniform dispersion (compared to HP-3, which is not smoothly dispersed), placing it in a range that

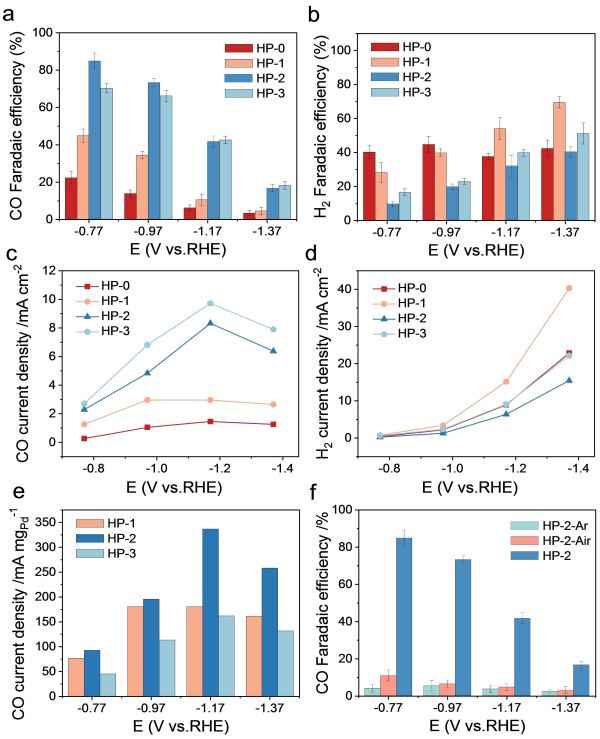

Figure 3. CO_2RR activities of samples in CO_2-saturated 0.5 M $KHCO_3$ solution with the flow rate of CO_2 gas maintained at 40 sccm. (a) FE for CO, (b) FE for H_2, (c) partial current density for CO production, (d) partial current density for H_2 production, and (e) Pd mass activity for CO for the prepared catalysts as a function of applied electrochemical potential. (f) FE for CO of HP-2 and its derivatives, obtained by pyrolysis in the air (HP-2-Air) and Ar (HP-2-Ar) atmospheres, as a function of applied electrochemical potential. The error bars were obtained from three independent experiments.

effectively balances the number of active sites with efficient mass transport. With increasingly negative polarization potentials, the FE of CO_2 to CO decreased while the FE of H_2 increased for all HP-1, HP-2 and HP-3 samples. In contrast, the Pd-free sample HP-0 exhibited an overall constant FE for H_2 production (~40 %) across applied potential, which can be ascribed to the formation of other gaseous products (CH_4 and C_2H_4) at more reductive potentials (Figure S9). The partial current densities for CO and H_2 production calculated from the respective FEs, are shown in Figures 3c, d. Overall, the partial current density for CO production initially increased at lower polarization potentials and then decreased at more negative potentials, i.e., −1.37 V_{RHE}. Concurrently, the partial current density for H_2 production increased dramatically when the applied potential was below −0.77 V_{RHE}. This can be ascribed to the limited mass transport of CO_2 in the electrolyte, which facilitates the hydrogen evolution reaction and the formation of other gaseous side products.[29] The influence of catalyst loading on current density and product selectivity was also investigated for HP-2 (Figure S10). The results indicate that catalyst overloading may decrease the CO partial current density due to charge transfer and mass transport limitations.

The stability of the catalyst was next investigated as a major limitation in aqueous electrochemistry with MOF-based systems. The X-ray diffraction patterns of HP-2 was recorded at various applied potentials from −0.77 to −1.37 V_{RHE} (Figure S11). While the diffraction peak intensity of the MOF weakened, the characteristic reflections remained observable, suggesting enduring crystalline MOF structures. The durability of HP-2 for CO_2RR was investigated by monitoring CO evolution for 6 h at −0.77 V_{RHE} and revealed a loss in FE from ~85 to 62 % (Figure S12). Post-catalysis X-ray photoelectron spectroscopy (XPS) analysis of the samples showed the formation of metallic Pd in line with the increased H_2 evolution and suggesting at a partial collapse of the MOF structure (Figure S13).

To obtain additional insights into the state of the catalyst during CO_2RR electrocatalysis at −0.77 V_{RHE}, we tracked the local atomic configuration and oxidation state of the Pd atoms, which are more readily reduced compared to Cu atoms, in HP-2 under in situ conditions as a representative. The schematic cell is presented in Figure 4a. Although the in situ data (Figure 4b) are significantly noisier than in the absence of an applied potential, there are no essential differences in both the XANES or EXAFS spectra in *k* and *R* space (Figures 4c–d). The first peak in the EXAFS modulus spectrum at 1.48 Å is ascribed to the Pd–O contribution, which remained unchanged. These imply that the HP-2 catalyst experiences no major reorganization under in situ conditions (−0.77 V_{RHE}).

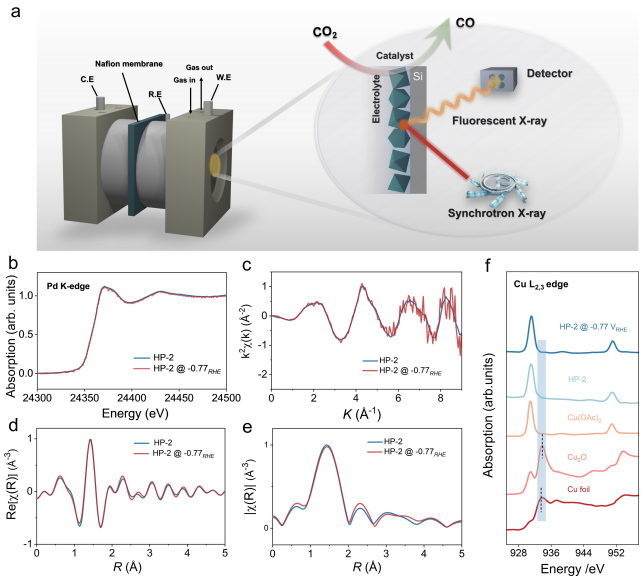

Figure 4. (a) Scheme of in situ cell which uses Ag/AgCl as reference electrode (R.E) and silicon wafer as work electrode (W.E) and counter electrode (C.E). (b) Comparison of in situ Pd K-edge XAFS spectra at −0.77 V_{RHE} with ex situ spectra. (c) Pd EXAFS data shown in *k* space. (d) The modulus part and (e) the real part of the Fourier-transformed (FT−) EXAFS signals in *R* space. Note that the Pd K-edge datasets here were measured on a different batch of samples and at a different facility compared to the Pd EXAFS shown in Figure 2. Additionally, the dehydration wash processes for this sample batch are relaxed, as the in situ conditions occur in an aqueous environment. Consequently, there are small discrepancies compared to Pd EXAFS shown in Figure 2. (f) Ex situ Cu L-edge XANES spectra were measured in total electron yield (TEY) mode.

Compared to the bulk-sensitive Pd- and Cu-XANES measured in transmission-mode, the L-edge XANES is more sensitive to the samples' surfaces.[30] The ex situ Cu L-edge XANES of the HP-2 catalyst was also employed to examine the oxidation state of Cu species before and after CO_2RR experiments. The Cu L-edge spectrum involves the Cu 2p→3d transition and core hole spin-orbit splitting of the spectrum into two peaks, namely the L_3- and L_2-edges centered at around 930 and 950 eV, respectively. Figure 4f presents the spectra of HP-2 before and after CO_2RR at −0.77 V_{RHE}, as well as those of $Cu(OAc)_2$, Cu_2O, and Cu foil as divalent, monovalent, and zero-valent references, respectively. Both Cu^{2+} and Cu^{+} have strong and well-resolved L_3 absorption edges at 930.8 and 933.7 eV, respectively, in agreement with values reported in the literature, while that of metallic Cu appears at around 933.5 eV.[31] Post-catalysis, the HP-2 trace showed spectral characteristics matching those of $Cu(OAc)_2$ and no obvious peaks around 933.5 (Cu^0) and 933.7 eV (Cu^+), suggesting no alteration of the MOF structure. Furthermore, post-electrolysis ^{1}H nuclear magnetic resonance (NMR) analysis of the electrolyte revealed no ligand (Figure S14), indicating no major leaching from the catalysts. Overall, these analyses infer that although HP-2 gradually degraded in the long-term test, the local Pd–Cu paddle wheel structures remain unaltered during the working electrochemical conditions investigated here. This further supports the catalytic nature of the bimetallic paddle wheel dimers of the MOF structure.

Building on the local atomic coordination results, DFT calculations were employed to investigate the underlying reaction mechanism for the enhanced CO_2 electroreduction selectivity (Figure 5, optimized configuration models are available in the Supporting Information). Cu–Cu and Pd–Pd homodimers and the Cu–Pd heterodimer were considered to account for all species potentially present in the structure after the partial metal cation substitution. The corresponding CO_2-binding scenarios were investigated by calculating the Gibbs free energy of the CO_2-reduction intermediate states (Figures 5a, b).

Across all samples, the highest free energy barrier in the reaction was the activation of CO_2 to form adsorbed *COOH. Replacing Cu by Pd significantly lowers the free energy barrier compared to that of homometallic Cu–Cu, with the homometallic Pd–Pd model exhibiting the lowest free energy barrier. The corresponding HER diagram showed the same trend toward H* adsorption, suggesting Pd introduction improves the overall reactivity of both CO_2RR and HER. Previous studies suggested that the difference between the limiting potentials for the CO_2RR and HER (i.e., $U_L(CO_2)$-$U_L(H_2)$), obtained from the free energies (see Supporting Information), can be applied as a reasonable descriptor for CO_2RR selectivity, with higher $U_L(CO_2)$-$U_L(H_2)$ values accounting for higher activity toward the CO_2RR over the HER.[32] Our calculations demonstrated in Figure 5c indicate that the Cu–Pd(Cu) moiety – i.e., the heterometallic Pd–Cu dimer with CO_2 binding at the Cu site – displays the highest $U_L(CO_2)$-$U_L(H_2)$ value, suggesting that

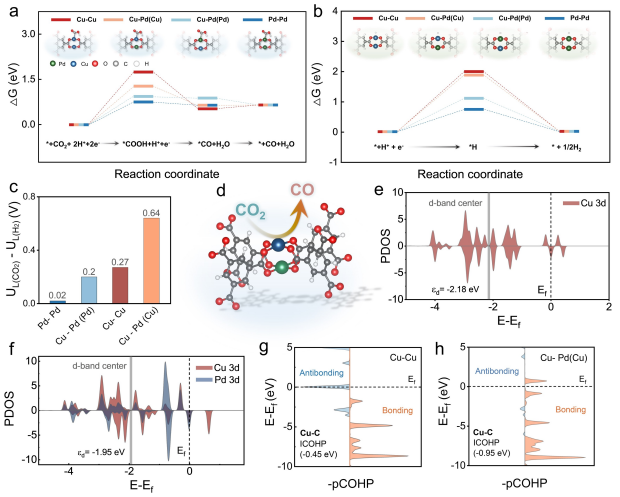

Figure 5. (a) Gibbs free energy along the CO_2 electroreduction pathway to CO on each site of the Cu–Cu, **Cu**-Pd, Cu-**Pd** (binding at the bolded element), and Pd–Pd dimer paddle wheel structure. Inserted pictures show the configuration of *COOH on different adsorption site. Green, Pd; blue, Cu; red, O; grey, C; white, H. (b) Gibbs free energy along the hydrogen evolution reaction pathway on each site (bold element) of Cu–Cu, **Cu**-Pd, Cu-**Pd** and Pd–Pd dimer paddle wheel structure. Insert pictures are configuration of *H on different adsorption sites (c) The limiting potential difference between CO_2RR and HER on Cu–Cu, **Cu**-Pd, Cu-**Pd** (binding at the bolded element), and Pd–Pd dimer paddle wheel structure (d) Scheme of CO_2 reduction on Cu site in the Cu–Pd dimer. Projected density of states of 3d orbitals of (e) the Cu atom in a Cu–Cu dimer and (f) the Pd atom in a Cu–Pd dimer. Projected crystal orbital Hamilton population (pCOHP) between the metal centers (g) Cu in a Cu–Cu dimer (h) Cu in a Cu–Pd dimer, with adsorbed COOH*.

this site provides the highest selectivity for the CO_2RR. In contrast, Pd–Pd displays little discrimination between the two reactions (The details of U_L for each reaction on different absorption sites can be seen in Table S3). Thus, these calculations, combined with the electrocatalysis results, indicate that Cu–Pd (Cu) is the primary selective active site in CO_2RR to CO (as the scheme shown in Figure 5d). To further evaluate the selectivity for CO over CH_4 and C_2H_4, we calculated the free energy barriers for *CO hydrogenation, C–C coupling, and CO desorption. The results shown in Figure S15 demonstrate that CO desorption from the surface is much more favorable compared to forming CH_4/C_2H_4 intermediate, which explains the high selectivity of HP-2 for CO over CH_4 and C_2H_4.

To better understand the adsorbate bonding strengths, we calculated the partial density of states of the adsorption configurations of the adsorbed COOH* and determined the energy positions of the d-band centers of the adsorption sites (Cu–Cu and Cu–Pd dimers), yielding values of −2.18 and −1.95 eV for Cu atoms, respectively (Figures 5e and 5f). Thus, we find that the Pd shifts the d-band center of the Cu atoms toward the Fermi level. As a result, the filling of the antibonding (d-σ)* state is decreased leading to a stronger binding of the adsorbate on Cu. The interaction between the metal center and the COOH* intermediate was analyzed utilizing the projected crystal orbital Hamilton population (pCOHP). The occupancy of the Cu-COOH* antibonding state exhibits a decrease from Cu–C in the Cu–Cu dimer to Cu–C in the Cu–Pd dimer (Figures 5g and **5h**), indicating an enhanced adsorption strength of the intermediates on Cu in the Cu–Pd model. Specifically, the integrated COHP (ICOHP) values were calculated to be −0.95 and −0.45 eV for the Cu–Pd and Cu–Cu models, respectively. This further demonstrates an optimized bonding/antibonding orbital population in the Cu–Pd model, which accounts for the enhanced adsorption strength of intermediates in the rate-determining step. Overall, these calculations suggest that Pd–Pd dimer will facilitate both HER and CO evolution in CO_2RR. However, the presence of Pd in the Cu–Pd structure will not only lower the energy barrier for the CO_2RR, but obvious enhance the key intermediate of COOH* adsorption on Cu sites, resulting in CO_2 selective reduced into CO. This insight helps to understand the effectiveness of MOF node engineering toward selective catalysis.

To further elucidate the role of the MOF matrix in catalysis, HP-2 was subjected to pyrolysis under Ar or air atmosphere at 700 or 400 °C, respectively. The selected temperatures were based on thermogravimetric analysis (TGA) curves (Figures S16–17) to ensure the complete decomposition and carbonization of the MOF to yield derived electrocatalysts. The obtained powders displayed metallic PdCu and Pd/CuO XRD patterns respectively (Figures S18–19). The resulting materials were investigated as CO_2RR catalysts under identical measurement conditions, with the results presented in Figure 3f. Both pyrolyzed samples exhibited significantly lower CO and higher H_2 FEs relative to HP-2. Moreover, the HP-2 mass partial current density (mass activity) for CO was 92.7 and 195.7 A g_{Pd}^{-1} at −0.77 and −1.17 V_{RHE}, respectively. It surpasses previously reported results for CuPd and other Pd alloy system catalysts (as summarized in Table S4), suggesting the atomic configuration of the intact Cu–Pd paddle wheel construct is essential for achieving higher CO selectivity and activity. These observations imply that a molecular level coordination network structure of the catalyst is advantageous not only for the rational design of selective electrocatalytic sites but also the enhancement of noble metal atom efficiency.

Conclusions

In summary, this study focused on the compositional modification of the model system HKUST-1 to rationalize and enhance the CO selectivity in Cu-based CO_2RR. Comprehensive characterization verified that a fraction of the Cu sites of the paddle wheel nodes located near the external surfaces of the MOF particles were successfully replaced by Pd, creating a Cu–Pd paddle-wheel dimer structure without the formation of metallic Pd. Benefiting from this MOF node modification, the resulting Cu–Pd catalyst not only showed significantly higher FE of CO (~85 %) than pure HKUST-1 (~28 %), but also excellent CO mass activity based on Pd. Moreover, the XAFS measurement verified that there is no obvious change in the Pd coordination environment under in situ conditions, which

provides a fundamental basis for catalytic reaction theoretical simulation. The following DFT calculations reveal that Pd played a crucial role in enhancing selectivity by affecting the COOH adsorption strength on the proximate Cu site, which ultimately lowered the energy barrier for CO_2RR. Overall, this work not only produced a PdCu core–shell MOF, but also improves the understanding MOF catalyst modulation and provides an approach for rationally-designed catalysts for enhanced selectivity in CO_2RR. Future improvements in current density and faradaic efficiency may be achieved by incorporating Cu-Pd paddle wheel nodes into robust 2D-type coordination networks, either deposited or directly grown as thin films on the working electrode surface. This offers a promising pathway for further enhancing CO_2RR selectivity and current density in CO_2 to CO conversion. Additionally, this approach can be applied to more chemically stable systems to develop commercially viable catalysts for other selective reactions.

Acknowledgements

R. R. Zhang and P. Ding are grateful for the PhD fellowships donated by the China Scholarship Council (CSC). P.D. and I.D.S. acknowledge support from the Deutsche Forschungsgemeinschaft (DFG, German Research Foundation) under Germany's Excellence Strategy–EXC 2089/1–390776260. Y. Liu acknowledge support from the National Natural Science Foundation of China (22303002). S.D.K and J. H acknowledge the use of resources of the Advanced Photon Source, a U.S. Department of Energy (DOE) Office of Science user facility at Argonne National Laboratory and is based on research supported by the U.S. DOE Office of Science-Basic Energy Sciences, under Contract No. DE-AC02-06CH11357. The authors thank the Munich Compact Light Source (MuCLS), beamline BL11B and BL14 W1 at Shanghai Synchrotron Radiation Facility (SSRF) and MCD-A and MCD-B (Soochow Beamline for Energy Materials) at National Synchrotron Radiation Laboratory (NSRL) in USTC for providing the beam time. This work was also supported by the User Experiment Assist System of SSRF. Numerical computations were performed on Hefei advanced computing center. Open Access funding enabled and organized by Projekt DEAL.

Conflict of Interest

The authors declare no conflict of interest.

Data Availability Statement

The data that support the findings of this study are available from the corresponding author upon reasonable request.

Keywords: Metal–Organic Frameworks · CO_2 electroreduction reaction · Pd/HKUST-1 · Cu–Pd paddlewheel structure

[1] a) C.-T. Dinh, T. Burdyny, M. G. Kibria, A. Seifitokaldani, C. M. Gabardo, F. P. G. de Arquer, A. Kiani, J. P. Edwards, P. De Luna, O. S. Bushuyev, *Science* **2018**, *360*, 783–787; b) S. Gao, Y. Lin, X. Jiao, Y. Sun, Q. Luo, W. Zhang, D. Li, J. Yang, Y. Xie, *Nature* **2016**, *529*, 68–71.
[2] S. Popović, M. Smiljanić, P. Jovanovič, J. Vavra, R. Buonsanti, N. Hodnik, *Angew. Chem. Int. Ed.* **2020**, *59*, 14736–14746.
[3] a) D. Kim, J. Resasco, Y. Yu, A. M. Asiri, P. Yang, *Nat. Commun.* **2014**, *5*, 4948; b) D. Gao, R. M. Arán-Ais, H. S. Jeon, B. Roldan Cuenya, *Nat. Catal.* **2019**, *2*, 198–210.
[4] a) Z. Yin, D. Gao, S. Yao, B. Zhao, F. Cai, L. Lin, P. Tang, P. Zhai, G. Wang, D. Ma, X. Bao, *Nano Energy* **2016**, *27*, 35–43; b) X. Zheng, Y. Ji, J. Tang, J. Wang, B. Liu, H.-G. Steinrück, K. Lim, Y. Li, M. F. Toney, K. Chan, Y. Cui, *Nat. Catal.* **2018**, *2*, 55–61; c) D. Gao, H. Zhou, J. Wang, S. Miao, F. Yang, G. Wang, J. Wang, X. Bao, *J. Am. Chem. Soc.* **2015**, *137*, 4288–4291.
[5] A. Goyal, G. Marcandalli, V. A. Mints, M. T. Koper, *J. Am. Chem. Soc.* **2020**, *142*, 4154–4161.
[6] a) Y. Pan, R. Lin, Y. Chen, S. Liu, W. Zhu, X. Cao, W. Chen, K. Wu, W.-C. Cheong, Y. Wang, *J. Am. Chem. Soc.* **2018**, *140*, 4218–4221; b) C. Lu, J. Yang, S. Wei, S. Bi, Y. Xia, M. Chen, Y. Hou, M. Qiu, C. Yuan, Y. Su, *Adv. Funct. Mater.* **2019**, *29*, 1806884.
[7] S. Back, M. S. Yeom, Y. Jung, *ACS Catal.* **2015**, *5*, 5089–5096.
[8] M. Valenti, N. P. Prasad, R. Kas, D. Bohra, M. Ma, V. Balasubramanian, L. Chu, S. Gimenez, J. Bisquert, B. Dam, *ACS Catal.* **2019**, *9*, 3527–3536.
[9] Y. Wang, H. Shen, K. J. Livi, D. Raciti, H. Zong, J. Gregg, M. Onadeko, Y. Wan, A. Watson, C. Wang, *Nano Lett.* **2019**, *19*, 8461–8468.
[10] a) K. Jiang, Y. Huang, G. Zeng, F. M. Toma, W. A. Goddard III, A. T. Bell, *ACS Energy Lett.* **2020**, *5*, 1206–1214; b) P. Ding, H. An, P. Zellner, T. Guan, J. Gao, P. Müller-Buschbaum, B. M. Weckhuysen, W. van der Stam, I. D. Sharp, *ACS Catal.* **2023**, *13*, 5336–5347.
[11] Y. Lum, B. Yue, P. Lobaccaro, A. T. Bell, J. W. Ager, *J. Phys. Chem. C* **2017**, *121*, 14191–14203.
[12] H. Yang, Y. Wu, G. Li, Q. Lin, Q. Hu, Q. Zhang, J. Liu, C. He, *J. Am. Chem. Soc.* **2019**, *141*, 12717–12723.
[13] a) P. C. Chen, C. Chen, Y. Yang, A. L. Maulana, J. Jin, J. Feijoo, P. Yang, *J. Am. Chem. Soc.* **2023**, *145*, 10116–10125; b) D. Kim, S. Yu, F. Zheng, I. Roh, Y. Li, S. Louisia, Z. Qi, G. A. Somorjai, H. Frei, L.-W. Wang, *Nat. Energy* **2020**, *5*, 1032–1042; c) J. C. Bui, C. Kim, A. J. King, O. Romiluyi, A. Kusoglu, A. Z. Weber, A. T. Bell, *Acc. Chem. Res.* **2022**, *55*, 484–494; d) P.-C. Chen, X. Liu, J. L. Hedrick, Z. Xie, S. Wang, Q.-Y. Lin, M. C. Hersam, V. P. Dravid, C. A. Mirkin, *Science* **2016**, *352*, 1565–1569; e) P.-C. Chen, J. S. Du, B. Meckes, L. Huang, Z. Xie, J. L. Hedrick, V. P. Dravid, C. A. Mirkin, *J. Am. Chem. Soc.* **2017**, *139*, 9876–9884; f) P.-C. Chen, M. Liu, J. S. Du, B. Meckes, S. Wang, H. Lin, V. P. Dravid, C. Wolverton, C. A. Mirkin, *Science* **2019**, *363*, 959–964; g) E. L. Clark, C. Hahn, T. F. Jaramillo, A. T. Bell, *J. Am. Chem. Soc.* **2017**, *139*, 15848–15857; h) C.-J. Chang, S.-C. Lin, H.-C. Chen, J. Wang, K. J. Zheng, Y. Zhu, H. M. Chen, *J. Am. Chem. Soc.* **2020**, *142*, 12119–12132.
[14] a) S. Ma, M. Sadakiyo, M. Heima, R. Luo, R. T. Haasch, J. I. Gold, M. Yamauchi, P. J. Kenis, *J. Am. Chem. Soc.* **2017**, *139*, 47–50; b) Y. Li, Z. Tian, L. Chen, *J. Phys. Chem. C* **2021**, *125*, 21381–21389; c) F.-Y. Zhang, T. Sheng, N. Tian, L. Liu, C. Xiao, B.-A. Lu, B.-B. Xu, Z.-Y. Zhou, S.-G. Sun, *Chem. Commun.* **2017**, *53*, 8085–8088; d) R. Jana, A. Bhim, P. Bothra, S. K. Pati, S. C. Peter, *ChemSusChem* **2016**, *9*, 2922–2927.
[15] Y. Jiang, Y. Wang, R. Chen, Y. Li, C. Li, *Energy Fuels* **2023**.

[16] a) L. Ma, C. Abney, W. Lin, *Chem. Soc. Rev.* **2009**, *38*, 1248–1256; b) Y. Liu, W. Xuan, Y. Cui, *Adv. Mater.* **2010**, *22*, 4112–4135; c) C. Wang, D. Liu, W. Lin, *J. Am. Chem. Soc.* **2013**, *135*, 13222–13234; d) S. Furukawa, J. Reboul, S. Diring, K. Sumida, S. Kitagawa, *Chem. Soc. Rev.* **2014**, *43*, 5700–5734; e) L. Zhang, H. B. Wu, X. W. Lou, *J. Am. Chem. Soc.* **2013**, *135*, 10664–10672.
[17] D. M. Shakya, O. A. Ejegbavwo, T. Rajeshkumar, S. D. Senanayake, A. J. Brandt, S. Farzandh, N. Acharya, A. M. Ebrahim, A. I. Frenkel, N. Rui, *Angew. Chem. Int. Ed.* **2019**, *58*, 16533–16537.
[18] Y. Liu, Y. Wang, S. Zhao, Z. Tang, *Small Methods* **2022**, *6*, 2200773.
[19] a) D. Senthil Raja, X. F. Chuah, S. Y. Lu, *Adv. Energy Mater.* **2018**, *8*, 1801065; b) F. Sun, G. Wang, Y. Ding, C. Wang, B. Yuan, Y. Lin, *Adv. Energy Mater.* **2018**, *8*, 1800584; c) W. Zhou, D. D. Huang, Y. P. Wu, J. Zhao, T. Wu, J. Zhang, D. S. Li, C. Sun, P. Feng, X. Bu, *Angew. Chem. Int. Ed.* **2019**, *58*, 4227–4231; d) L. Tang, M. Cai, M. Zhang, X. Chen, Z. Cai, *RSC Adv.* **2022**, *12*, 25112–25117.
[20] H. Zhong, M. Ghorbani-Asl, K. H. Ly, J. Zhang, J. Ge, M. Wang, Z. Liao, D. Makarov, E. Zschech, E. Brunner, *Nat. Commun.* **2020**, *11*, 1409.
[21] R. Iqbal, M. B. Akbar, A. Ahmad, A. Hussain, N. Altaf, S. Ibraheem, G. Yasin, M. A. Khan, M. Tabish, A. Kumar, *Adv. Mater. Interfaces* **2022**, *9*, 2101505.
[22] a) D.-H. Nam, O. S. Bushuyev, J. Li, P. De Luna, A. Seifitokaldani, C.-T. Dinh, F. P. García de Arquer, Y. Wang, Z. Liang, A. H. Proppe, *J. Am. Chem. Soc.* **2018**, *140*, 11378–11386; b) J. Albo, D. Vallejo, G. Beobide, O. Castillo, P. Castano, A. Irabien, *ChemSusChem* **2017**, *10*, 1100–1109.
[23] J. Albo, M. Perfecto-Irigaray, G. Beobide, A. Irabien, *J. CO2 Util.* **2019**, *33*, 157–165.
[24] a) X. Han, C. Yu, J. Yang, C. Zhao, H. Huang, Z. Liu, P. M. Ajayan, J. Qiu, *Adv. Mater. Interfaces* **2016**, *3*, 1500782; b) F. Zheng, W. Zhang, X. Zhang, Y. Zhang, W. Chen, *Adv. Funct. Mater.* **2021**, *31*, 2103318.
[25] R. Zhang, L. Hu, S. Bao, R. Li, L. Gao, R. Li, Q. Chen, *J. Mater. Chem. A* **2016**, *4*, 8412–8420.
[26] P. Guo, C. Froese, Q. Fu, Y.-T. Chen, B. Peng, W. Kleist, R. A. Fischer, M. Muhler, Y. Wang, *J. Phys. Chem. C* **2018**, *122*, 21433–21440.
[27] B. Ravel, M. Newville, *J. Synchrotron Radiat.* **2005**, *12*, 537–541.
[28] R. J. Meyer, S. R. Bare, G. A. Canning, J. G. Chen, P. M. Chu, A. S. Hock, A. S. Hoffman, A. M. Karim, S. D. Kelly, Y. Lei, *J. Catal.* **2024**, 115369.
[29] M. R. Singh, E. L. Clark, A. T. Bell, *Phys. Chem. Chem. Phys.* **2015**, *17*, 18924–18936.
[30] S. Schroeder, G. Moggridge, R. Ormerod, T. Rayment, R. Lambert, *Surf. Sci.* **1995**, *324*, L371–L377.
[31] a) R. Sarangi, N. Aboelella, K. Fujisawa, W. B. Tolman, B. Hedman, K. O. Hodgson, E. I. Solomon, *J. Am. Chem. Soc.* **2006**, *128*, 8286–8296; b) A. Davó-Quiñonero, E. Bailon-Garcia, S. Lopez-Rodriguez, J. n. Juan-Juan, D. Lozano-Castello, M. García-Melchor, F. C. Herrera, E. Pellegrin, C. Escudero, A. Bueno-Lopez, *ACS Catal.* **2020**, *10*, 6532–6545.
[32] C. Shi, H. A. Hansen, A. C. Lausche, J. K. Nørskov, *Phys. Chem. Chem. Phys.* **2014**, *16*, 4720–4727.

Manuscript received: August 1, 2024
Accepted manuscript online: October 24, 2024
Version of record online: November 16, 2024